The analysis of initial Juno magnetometer data using a sparse magnetic field representation

Moore, Kimberly M.; Bloxham, Jeremy; Connerney, John E. P.; Jørgensen, John Leif; Merayo, José M.G.

Published in:
Geophysical Research Letters

Link to article, DOI:
10.1002/2017GL073133

Publication date:
2017

Document Version
Publisher's PDF, also known as Version of record

AGU PUBLICATIONS

Geophysical Research Letters

RESEARCH LETTER
10.1002/2017GL073133

Special Section:
Early Results: Juno at Jupiter

The analysis of initial Juno magnetometer data using a sparse magnetic field representation

Kimberly M. Moore[1,2], Jeremy Bloxham[1], John E. P. Connerney[3,4], John L. Jørgensen[5], and José M. G. Merayo[5]

[1]Department of Earth and Planetary Sciences, Harvard University, Cambridge, Massachusetts, USA, [2],Now at Cambridge, Massachusetts, USA, [3]Solar System Exploration Division, Planetary Magnetospheres Laboratory, NASA Goddard Space Flight Center, Greenbelt, Maryland, USA, [4]Space Research Corporation, Annapolis, Maryland, USA, [5]Measurement and Instrumentation Systems, National Space Institute, Technical University of Denmark, Kongens Lyngby, Denmark

Key Points:
- Analysis of magnetometer data from Juno's first perijove pass at Jupiter
- Application of an elastic net regression to enhance existing field models

Correspondence to:
K. M. Moore,
kimberlymoore@g.harvard.edu

Citation:
Moore, K. M., J. Bloxham, J. E. P. Connerney, J. L. Jørgensen, and J. M. G. Merayo (2017), The analysis of initial Juno magnetometer data using a sparse magnetic field representation, *Geophys. Res. Lett.*, *44*, 4687–4693, doi:10.1002/2017GL073133.

Received 17 FEB 2017
Accepted 19 APR 2017
Published online 25 MAY 2017

Abstract The Juno spacecraft, now in polar orbit about Jupiter, passes much closer to Jupiter's surface than any previous spacecraft, presenting a unique opportunity to study the largest and most accessible planetary dynamo in the solar system. Here we present an analysis of magnetometer observations from Juno's first perijove pass (PJ1; to within 1.06 R_J of Jupiter's center). We calculate the residuals between the vector magnetic field observations and that calculated using the VIP4 spherical harmonic model and fit these residuals using an elastic net regression. The resulting model demonstrates how effective Juno's near-surface observations are in improving the spatial resolution of the magnetic field within the immediate vicinity of the orbit track. We identify two features resulting from our analyses: the presence of strong, oppositely signed pairs of flux patches near the equator and weak, possibly reversed-polarity patches of magnetic field over the polar regions. Additional orbits will be required to assess how robust these intriguing features are.

Plain Language Summary We analyze magnetic field data from the NASA Juno spacecraft's first orbital pass around Jupiter. Juno passes almost 10 times closer to Jupiter than any previous spacecraft, providing a unique look into the planet's physics. We use a new math technique to model the field near the orbit, providing a high-resolution enhancement to existing models in the regions where we have new data from the Juno Mission. The results have implications for the solid/rocky core of Jupiter, and the physics of how Jupiter generates its magnetic field.

1. Introduction

Magnetic field data from Juno's first close passage just above Jupiter's atmosphere [*Connerney et al.*, 2017] indicate that Jupiter's magnetic field is both much stronger and more spatially complex than indicated by previous models such as VIP4 [*Connerney et al.*, 1998]. Current models of Jupiter's main field use two primary sources of data. The first is in situ magnetometer data from the Pioneer 10 and 11, Voyager 1 and 2, and Ulysses missions (flybys) and the Galileo mission (equatorial orbiter). This led to spherical harmonic models such as the O6 model [*Connerney*, 1992] and the JCF/JSV models [*Ridley and Holme*, 2016]. The second set of observations useful for magnetic field modeling followed the discovery of infrared [*Connerney et al.*, 1993] and ultraviolet [*Clarke et al.*, 1996] emission at the foot of the Io flux tube in Jupiter's polar ionosphere. These localized emission features constrain the magnetic field geometry, tracing charged particle trajectories from Io and other Jovian moons to Jupiter's polar ionosphere. This approach, coupled with in situ data, was employed to create spherical harmonic degree 4 or 5 models such as VIP4 [*Connerney et al.*, 1998], VIT4 [*Connerney*, 2007], and extensions such as VIPAL [*Hess et al.*, 2011] that employ additional constraints.

NASA's Juno Mission has the potential to greatly improve current knowledge of Jupiter's magnetic field and was designed to provide global mapping of the magnetic field via 30 close periapsis passes equally spaced in longitude [*Connerney et al.*, 2017]. Prior missions had limited observational coverage in both space and time. The Pioneer 11 spacecraft provided the closest observations, passing to within about 43,000 km of the cloud tops (excepting Galileo's intentional deorbit into Jupiter's clouds). In contrast, Juno's closest approach at PJ1

was at an altitude of 4200 km, along a pole to pole track. In this paper we ask what additional magnetic field structure (beyond that contained in the VIP4 model field) at Jupiter's surface is necessary to explain the PJ1 observations (see *Bolton et al.* [2017] for an overview of these observations).

2. Method

Ordinarily, magnetic field models are derived by expanding the magnetic field potential V in surface spherical harmonics and then solving for the coefficients in the expansion. Specifically, with $\mathbf{B}(r,\theta,\phi) = -\nabla V(r,\theta,\phi)$ we have

$$V(r,\theta,\phi) = a\sum_{l=1}^{L}\sum_{m=0}^{l}\left(\frac{a}{r}\right)^{l+1}\left[g_l^m\cos m\phi + h_l^m\sin m\phi\right]P_l^m(\cos\theta) \tag{1}$$

where r,θ,ϕ are spherical polar coordinates, a is a reference value of r (e.g., a = 1.0 R_J, where we use R_J = 71,398 km), and P_l^m is a Gauss-Schmidt normalized associated Legendre polynomial.

The coefficients in the expansion may be sought by a variety of methods: most simply, the expansion is truncated at low degree L and the resulting overdetermined problem is solved using least squares. Such an approach would be appropriate only if the actual field could be well described by a low degree and order model and if the observations are sufficient to constrain the model parameters. Of course, there is no a priori reason why a planetary magnetic field should be such that it could be represented by a model truncated at a small value of L; instead, planetary magnetic fields are likely to be more complex, so that a large value of L is required to adequately represent the field. Then, the observations will not be sufficient to uniquely determine all the model parameters, resulting in an underdetermined problem. In such cases (e.g., a close flyby trajectory) methods such as singular value decomposition have been used to find partial solutions, identifying those combinations of coefficients that are well determined [*Connerney*, 1981]. The coefficients that can be uniquely determined are identified by inspection of the resolution matrix, a function of the number of eigenvectors admitted in the partial solution. Alternatively, most work over the last few decades has instead employed some form of regularization [e.g., *Shure et al.*, 1982] by minimizing, for example, a quadratic norm of the solution, which gives rise to smooth solutions.

Recently, *Bolton et al.* [2017] published a comparison of PJ1 magnetometer data with the fit by various models, including VIP4. It is clear, though not unexpected, that the data are not well fitted by models of this type, especially in equatorial latitudes where Juno reaches perijove, though there is also a systematic misfit at higher latitudes. What additional magnetic field structure must be added to VIP4 to adequately fit the data?

We note that whatever additional structure is required will necessarily be localized along the spacecraft track. To appreciate this, consider the magnetic field $\mathbf{B}$ at a point (r,θ,ϕ) along the track of the spacecraft: we can write $\mathbf{B}(r,\theta,\phi)$ as an integral of the magnetic field over a surface at radius r' [*Gubbins and Roberts*, 1983]. For example, for the radial component of the field

$$B_r(r,\theta,\phi) = \int_0^{2\pi}\int_0^{\pi} B_r\left(r',\theta',\phi'\right)G_r(\Psi)\sin\theta' d\theta' d\phi' \tag{2}$$

where the Green's function is given by

$$G_r(\Psi) = \frac{b^2}{4\pi}\frac{(1-b^2)}{f^3} \tag{3}$$

with $b = r'/r$,

$$f(\Psi,r) = (1-2b\cos(\Psi)+b^2)^{1/2} \tag{4}$$

and Ψ is the angle between $\mathbf{r} = (r,\theta,\phi)$ and $\mathbf{r}' = (r',\theta',\phi')$. See *Gubbins and Roberts* [1983] and *Johnson and Constable* [1997] for the other components of the field.

In Figure 1 we show the Green's functions for r'=0.85R_J (the putative upper boundary of the dynamo region, *Smoluchowski* [1975]) and r = 1.06R_J (corresponding to perijove) and r =1.97R_J (corresponding to a near polar point). The half amplitude half width is approximately 10° for r = 1.06 R_J, showing that the resolution at perijove is in a band approximately 10° either side of the track. At the poles that band increases in half width to approximately 30°. Accordingly, we expect to be able to explain the difference between VIP4 and the PJ1 observations with structure confined to a band near the spacecraft track. Put simply, we seek a magnetic field model which when added to VIP4 provides an adequate fit to the data.

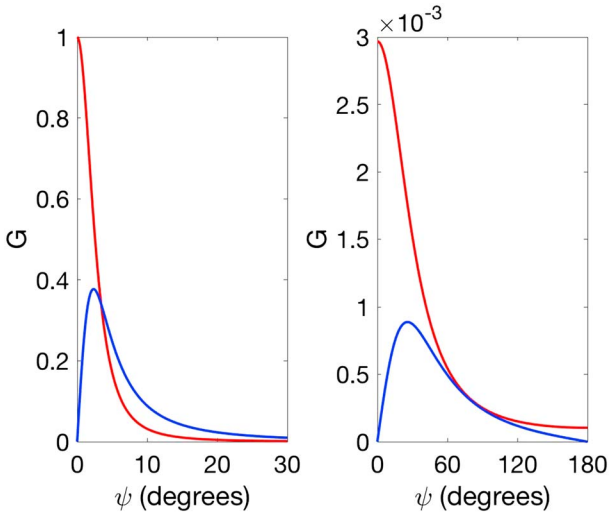

Figure 1. Green's functions corresponding to $r' = 0.85\ R_J$ for the radial and horizontal fields, G_r (red) and G_h (blue). (left) The Green's functions at perijove ($r = 1.06\ R_J$) and (right) those at a near polar point ($r = 1.97\ R_J$). Note that these Greens functions are normalized; all values are scaled to G_r at perijove, $1.06\ R_J$.

What properties should this model have? Foremost, it should only add structure that is required to fit the data: thus, away from the track it should be zero (so VIP4 is left unchanged in areas where the PJ1 data have no resolution), and near the track, we prefer models that are in some sense smooth. Given that we seek a model with these particular spatial attributes, it seems reasonable that we should use a spatial rather than spectral representation of the field. This point will become much clearer as we proceed, but in order to do so, we need to adopt a field representation.

We represent the magnetic field on the surface at r' by a tessellation of 10,000 magnetic elements on a sphere, where the magnetic field within each element of the tessellation is uniform. To form the tessellation we first find a set of nearly uniformly distributed points on the surface, using an algorithm that minimizes the Coulomb potential of the set of points [*Semechko*, 2012]; we then calculate approximately uniform surface elements by finding the Voronoi cell corresponding to each point, using an algorithm by *Luong* [2013]. Similar representations of the magnetic field using surface elements have been used previously; see, for example, *Constable et al.* [1993] and *Stockmann et al.* [2009]. The radial magnetic field at a point **r** resulting from this set of magnetic field elements on the surface is readily calculated using equation (2) or similar equations for the other components of the magnetic field.

First, we remove from the Juno PJ1 magnetometer data the vector field calculated using the VIP4 model, creating a data set of residuals. Next, we solve for the magnetic field within each surface element that best fits the residual data set; however, in doing so, we use a method (described below) that ensures that the value of the magnetic field in a particular surface element will be identically zero unless the residual data require otherwise. Finally, we add the set of nonzero magnetic field elements to VIP4. The result can be thought of as an enhancement of VIP4: where the PJ1 data require changes to VIP4 to fit the data, the elastic net will be nonzero, thus adding magnetic field elements to VIP4 and revealing new structure. Where the PJ1 data do not require changes to VIP4, VIP4 is left unchanged.

One approach to finding solutions with the property that an element is identically zero unless the data demand otherwise is to regularize the solution using an L1-norm. L1-norm regularization has been widely used, in fields ranging from genetics [*Heslot et al.*, 2012] to remote sensing [*Mercer et al.*, 2011]. Then, we would minimize an objective function of the form

$$\|\boldsymbol{\gamma} - \mathbf{G}\mathbf{m}\|^2 + \lambda\|\mathbf{m}\|_1 \tag{5}$$

where $\boldsymbol{\gamma}$ is a data vector comprised of the residual magnetic field measurements described above, **m** is a vector comprised of the radial magnetic field value in each surface element, G is a matrix with elements derived from the Green's functions, and λ is a regularization parameter.

However, this approach yields solutions which, for our application, would also have an undesirable property. Suppose the residual magnetic field measurements require that the magnetic field be nonzero within some particular region. The L1-norm then tends to yield a solution in which one surface element within the region is nonzero, with the other elements set to be zero. In other words, within a region in which the magnetic surface elements are correlated, generally only one such element would be selected to be nonzero. A variant of L1-norm regularization alleviates this shortcoming.

Zou and Hastie [2005] introduced the elastic net, which is a combination of L1 and L2 regularizations. The elastic net tends instead to select groups of correlated elements to be nonzero, rather than a single element

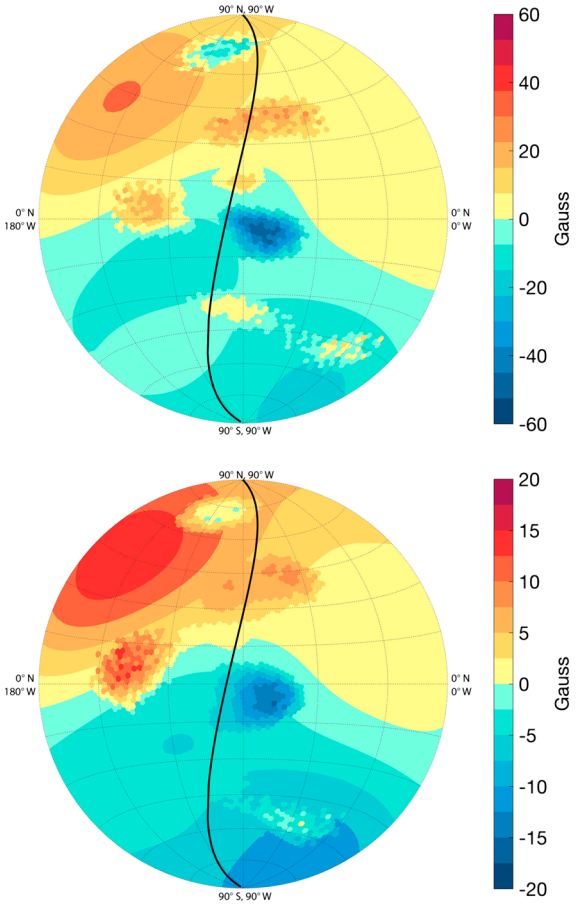

Figure 2. Models of the radial magnetic field, B_r, (top) at $r' = 0.85\ R_J$ and (bottom) at $r' = 1R_J$. The two models are the sum of VIP4 evaluated at the given value of r' and our elastic net fit to the VIP4 residuals, with the norm having been applied at the respective radii. Note that field intensity is higher in the top plot since it is plotted at a smaller radius. The Juno PJ1 track is denoted by the thin black line (orbit crossing the equator at longitude 96° west). The models are plotted using a Lambert equal area azimuthal projection centered on longitude 90° west in System III W coordinates. Note only one hemisphere is shown.

from the group. For the elastic net, the objective function becomes

$$\|\boldsymbol{\gamma} - \mathbf{G}\mathbf{m}\|^2 + \lambda \left[\alpha \|\mathbf{m}\|_1 + (1-\alpha)\|\mathbf{m}\|_2^2\right] \quad (6)$$

By varying the parameter α, we can adjust the properties of the solution, ranging from purely L1 solutions at $\alpha = 1$ to purely L2 solutions at $\alpha = 0$. We minimize this objective function using the numerical package glmnet [*Friedman et al.*, 2007; *Tibshirani et al.*, 2010; *Friedman et al.*, 2010].

Our choice to represent the field using a spherical tessellation makes the implementation of the elastic net straightforward, although other parameterizations could be used (for example, harmonic splines [*Shure et al.*, 1982], equivalent source dipole methods [*Oliviera et al.*, 2015], wavelet methods [*Holschneider et al.*, 2003], or spherical Slepian functions [*Simons et al.*, 2006]), though their implementation would be considerably more complicated or numerically expensive. Indeed, even surface spherical harmonics could be used, though then the expansion would have to be extended to extremely high degree to find a solution adequately approximating the desired properties. For other examples of a tessellation basis, see *Constable et al.* [1993] and *Stockmann et al.* [2009].

3. Results and Conclusions

We select PJ1 data with $r \leq 2.2\ R_J$ and at a sampling rate of 1 Hz. This gives a data set of 6966 three-component measurements of the magnetic field.

In Figure 2 we show our two preferred solutions, one at $r' = 0.85\ R_J$, and one at $r' = 1\ R_J$ (see also Figure 4 (bottom left) for this $0.85R_J$ model plotted using a different colorscale). While the two solutions are slightly different, the models appear to have broadly the same characteristics when regularized at either altitude. We caution that VIP4 was regularized at $1R_J$ and not originally intended for downward continuation below that level (this may impact the plots of VIP4 at the dynamo surface, but not our solutions or fit to the data, which rely on upward continuing VIP4 to satellite altitude).

In Figure 3, we show the fit of our $r' = 0.85\ R_J$ model (as pictured in Figure 2). Note that the model and data are almost indistinguishable from each other, showing a very good fit. The misfit is almost always below 1% for any given data point. Indeed, both the $r' = 0.85\ R_J$ and $r' = 1\ R_J$ models reduce the total variance by more than 99% when compared to VIP4 (where variance is the sum squared of the unweighted RMS misfit). The weighted RMS misfit of the solutions is defined as

$$w_{\mathrm{RMS}}^2 = \frac{n}{n-1} \frac{\sum_{i=1}^{n} \left(\frac{e_i}{\sigma_i}\right)^2}{\sum_{i=1}^{n} \frac{1}{\sigma_i^2}} \quad (7)$$

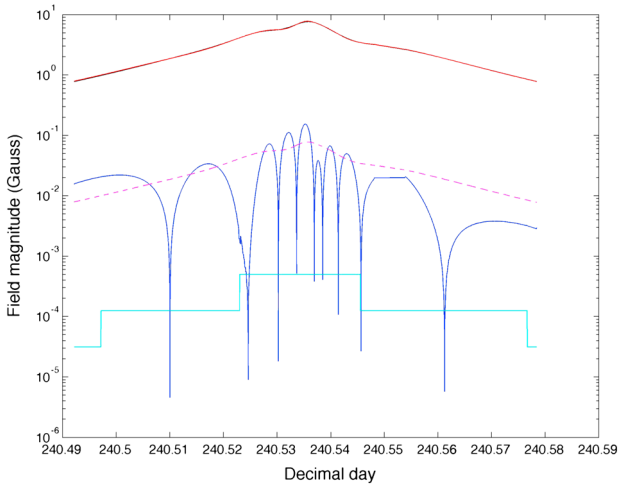

Figure 3. Comparison of $|B|$ for our model to PJ1 data ($r' = 0.85\ R_J$, $\alpha = 0.01$, and $\lambda = 0.25$). We show the Juno spacecraft observations (red) against the model (black). The two lines are nearly indistinguishable. We also plot the misfit (dark blue), as well as the 1% threshold for misfit to PJ1 data (magenta, dashed), and the quantization range of the magnetometer (cyan). The quantization range of the magnetometer can be thought of as a minimum error bound on the data, if no other sources of error are present. A 30 s smoothing has been applied to residuals.

with e_i representing the difference between the ith data point and the model and σ_i equal to the quantization error. The w_{RMS} of the VIP4 model to the data is 0.59 Gauss, while both the $r' = 0.85\ R_J$ and $r' = 1\ R_J$ models shown in Figure 2 have a w_{RMS} of 0.031 Gauss. We note that we specifically selected a conservative model. While models with lower misfit exist using our methodology (which would be closer to the quantization error bound on the data), we did not want to overfit any potential sources of noise that may be revealed by future orbits.

3.1. Choice of Regularization Parameters

The choice of values of the regularization parameters α and λ is subjective since a range of solutions provide adequate fits to the data. We illustrate this further by providing additional models with a range of α and λ. Figure 4 shows a survey of models in parameter space, keeping the w_{RMS} misfit to similar levels. All models are solved for and plotted at the dynamo surface, $r' = 0.85R_J$. Note that the colorbar is held constant for ease of comparison, but some models may plot beyond the scale. We remind the reader that $\alpha = 1$ represents a pure L1 norm, $\alpha = 0$ a pure L2 norm, and intermediate values mixed L1/L2 norms (see equation (6)).

The three models range from a sparser, mostly L1-norm dominated solution with the highest value of α of the three models, $\alpha = 0.09$ (Figure 4 (top), Model 1), to an intermediate case at $\alpha = 0.01$ (Figure 4 (bottom left), Model 2), and to a smoother solution, closer to a pure L2-norm model at $\alpha = 9\times10^{-4}$ (Figure 4 (bottom right), Model 3). Model 2 is the same as our preferred solution at $0.85R_J$, plotted as the top model in Figure 2. We note the overall physical features appear to be consistent across models; all models show reversed flux at the poles, as well as the presence of strong equatorial flux spots. Changing the regularization parameters does not remove these features nor move them to significantly different latitudes or longitudes. In this sense, the strong equatorial patches and reversed polar flux could be said to be robust features of the parameter space for this particular data set. However, the form of these overall patches does appear to change. In particular, there is a trade-off between the spatial extent of the features and their amplitude: intense, concentrated features (a more L1-norm based solution, like Model 1) fit the data as well as less intense but broader features (a more L2-norm based solution, like Model 3).

Our preferred solution at $0.85R_J$ (Figures 2 (top) and 4 (bottom left)) satisfies our criterion that the solution is sparse, with no structure added to VIP4 far from the spacecraft track (thus, Model 3 is too diffuse). More subjectively, it satisfies an a priori bias for large-scale structure rather than isolated, highly concentrated structure (Model 1 fails this requirement). Thus, satisfying the first criterion supports the choice of λ and the second our choice of α. A pure-L1 or pure-L2 solution could also be generated, but we note that these solutions would fail to meet our criteria for the same reasons as Models 1 and 3. However, given the subjectivity in these regularization parameter choices, it is important to note that the amplitude of the structure seen in Figure 2 is not robust nor is small-scale structure at the level of individual pixels. The overall large-scale pattern, though, is more robust than the amplitude and is mostly independent of regularization parameter choice.

3.2. Interpretation and Conclusions

We note two particular features of the structures shown in Figure 2. First, the appearance of strong patches of oppositely signed magnetic flux near the equator, which is suggestive of flux expulsion [*Allan and Bullard*, 1958]. The negatively signed patch just to the east of the track is particularly well resolved, as fortuitously it

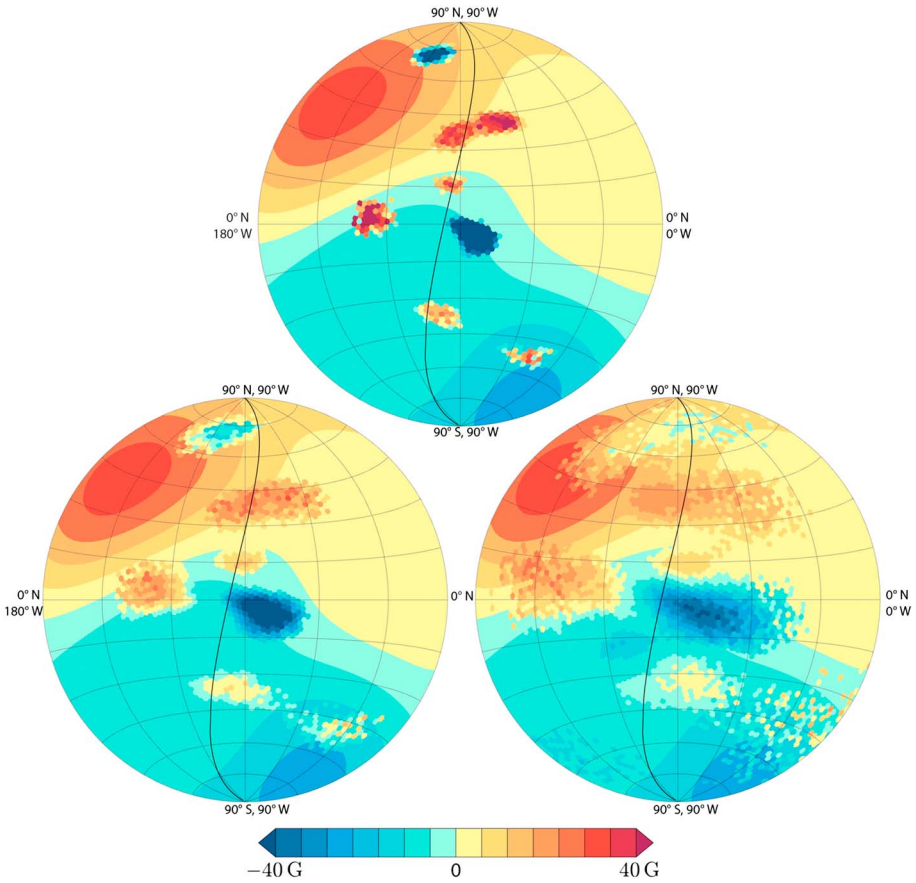

Figure 4. Models of the radial magnetic field, B_r, at $r' = 0.85\ R_J$ for a range of regularization parameters. (top) Model 1, with $\alpha = 0.09$, $\lambda = 0.05$, $w_{\mathrm{RMS}} = 0.033$ Gauss. Model 1 uses the highest value of α of the three models. The total B_r field values range from +70 to −117 Gauss. Note that the original VIP4 field values only ranged from +26 to −19 Gauss when plotted at this radius (0.85 R_J). (bottom left) Model 2, with $\alpha = 0.01$, $\lambda = 0.25$, $w_{\mathrm{RMS}} = 0.031$ Gauss. This model is the same as our $0.85R_J$ model from the main text, replotted here in this new colorscale for ease of comparison. The field values range from +29 to −59 Gauss. (bottom right) Model 3 with $\alpha = 9 \times 10^{-4}$, $\lambda = 0.5$, and $w_{RMS} = 0.029$ Gauss. The field values range from +28 to −42 Gauss.

would seem that Juno flew close to this patch. The field lines that enter the core through this patch must exit the core to the west, in order to explain the strong positive B_ϕ observed in this region, hence our association of the positively signed patch to the west (and slightly to the north) as the region in which these field lines exit the core. Second, the appearance of weak, and possibly even reversed, flux in polar regions, particularly near the north pole, which is suggestive of the dynamical influence of a tangent cylinder associated with a solid core [*Gubbins and Bloxham*, 1987]. While others have proposed low flux anomalies in Jupiter's polar regions [*Grodent et al.*, 2008], including in relation to the tangent cylinder around an inner core [*Ridley and Holme*, 2016], we emphasize that the PJ1 data are not well fitted within about $1.3R_J$ by previous models [*Bolton et al.*, 2017]. Owing to the increase in altitude by almost $1R_J$ of Juno from the equator to the poles, we have more confidence in our interpretation of the equatorial features than the polar features. More passes are required to adequately map the Jovian magnetic field for future comparison with dynamo models: fortunately, the Juno mission is designed to do just that.

Acknowledgments
We thank the many people who have contributed to making the Juno mission, led by Scott Bolton of Southwest Research Institute, a success. The Juno mission is funded by NASA and is part of the New Frontiers Program. We also thank Brendan Meade for many helpful discussions regarding this work and Richard Holme and an anonymous reviewer for their helpful suggestions. K.M. is supported by the Department of Defense (DoD) through the National Defense Science and Engineering Graduate Fellowship (NDSEG) Program. The Juno data used in this study will be made available through the Planetary Data System (PDS).

References

Allan, D. W., and E. Bullard (1958), Distortion of a toroidal field by convection, *Rev. Mod. Phys.*, *30*(3), 1087–1088, doi:10.1103/RevModPhys.30.1087.

Bolton, S. J., et al. (2017), Jupiter's interior and deep atmosphere: The first close polar pass with the Juno spacecraft, *Science*, doi:10.1126/science.aal2108, in press.

Clarke, J. T., et al. (1996), Far-ultraviolet imaging of Jupiter's aurora and the Io "footprint" with the hubble space telescope wide field planetary camera 2, *Science*, *274*, 404–409.

Connerney, J. (1992), Doing more with Jupiter's magnetic field, in *Planetary Radio Emissions III*, edited by H. O. Rucker, S. J. Bauer, and M. L. Kaiser, pp. 13–33, Austria Acad. of Sci. Press, Vienna.
Connerney, J. E. P. (1981), The magnetic field of Jupiter: A generalized inverse approach, *J. Geophys. Res.*, *86*(A9), 7679–7693.
Connerney, J. E. P. (2007), Planetary magnetism, *Treatise Geophys.*, *10*, 243–280.
Connerney, J. E. P., R. Baron, T. Satoh, and T. Owen (1993), Images of excited H3+ at the foot of the Io flux tube in Jupiter's atmosphere, *Science*, *262*, 1035–1038.
Connerney, J. E. P., M. H. Acuña, N. F. Ness, and T. Satoh (1998), New models of Jupiter's magnetic field constrained by the Io flux tube footprint, *J. Geophys. Res.*, *103*(A6), 11,929–11,939, doi:10.1029/97JA03726.
Connerney, J. E. P., et al. (2017), The Juno magnetic field investigation, *Space Sci. Rev.*, doi:10.1007/s11214-017-0334-z, in press.
Constable, C. G., R. L. Parker, and P. B. Stark (1993), Geomagnetic field models incorporating frozen-flux constraints, *Geophys. J. Int.*, *113*(2), 419–433, doi:10.1111/j.1365-246X.1993.tb00897.x.
Friedman, J., T. Hastie, H. Hofling, and R. Tibshirani (2007), Pathwise coordinate optimization, *Ann. Appl. Stat.*, *1*, 302–332.
Friedman, J., T. Hastie, and R. Tibshirani (2010), Regularization paths for generalized linear models via coordinate descent, *J. Stat. Softw.*, *33*(1), 1–22.
Grodent, D., B. Bonfond, J.-C. Gerard, A. Radioti, J. Gustin, J. T. Clarke, J. Nichols, and J. E. P. Connerney (2008), Auroral evidence of a localized magnetic anomaly in Jupiter's northern hemisphere, *J. Geophys. Res.*, *113*, A09201, doi:10.1029/2008JA013185.
Gubbins, D., and J. Bloxham (1987), Morphology of the geomagnetic field and implications for the geodynamo, *Nature*, *325*(6104), 509–511, doi:10.1038/325509a0.
Gubbins, D., and N. Roberts (1983), Use of the frozen flux approximation in the interpretation of archaeomagnetic and palaeomagnetic data, *Geophys. J. Int.*, *73*(3), 675–687, doi:10.1111/j.1365-246X.1983.tb03339.x.
Heslot, N., H.-P. Yang, M. E. Sorrells, and J.-L. Jannink (2012), Genomic selection in plant breeding: A comparison of models, *Crop Sci.*, *52*, 146–160.
Hess, S. L. G., B. Bonford, P. Zarka, and D. Grodent (2011), Model of the Jovian magnetic field topology constrained by the Io auroral emissions, *J. Geophys. Res.*, *116*, A05217, doi:10.1029/2010JA016262.
Holschneider, M., A. Chambodut, and M. Mandea (2003), From global to regional analysis of the magnetic field on the sphere using wavelet frames, *Phys. Earth Planet. Inter.*, *135*(2–3), 107–124, doi:10.1016/S0031-9201(02)00210-8.
Johnson, C. L., and C. G. Constable (1997), The time-averaged geomagnetic field: Global and regional biases for 0–5 Ma, *Geophys. J. Int.*, *131*(3), 643–666, doi:10.1111/j.1365-246X.1997.tb06604.x.
Luong, B. (2013), *Voronoi Sphere*, Mathworks File Exchange. [Available at https://www.mathworks.com/matlabcentral/fileexchange/40989-voronoi-sphere, accessed 2017.]
Mercer, L. D., A. A. Szpiro, J. Lindstrom, S. D. Adar, R. W. Allen, E. L. Avol, A. P. Oron, T. Larson, L.-J. S. Liu, and J. D. Kaufman (2011), Comparing universal kriging and land-use regression for predicting concentrations of gaseous oxides of nitrogen (NOx) for multi-ethnic study of atherosclerosis and air pollution (mesa air), *Atmos. Environ.*, *45*, 4412–4420.
Oliviera, J. S., B. Langlais, M. A. Pais, and H. Amit (2015), A modified Equivalent Source Dipole method to model partially distributed magnetic field measurements, with application to Mercury, *J. Geophys. Res. Planets*, *120*, 1075–1094, doi:10.1002/2014JE004734.
Ridley, V. A., and R. Holme (2016), Modeling the Jovian magnetic field and its secular variation using all available magnetic field observations, *J. Geophys. Res. Planets*, *121*, 309–337, doi:10.1002/2015JE004951.
Semechko, A. (2012), *Suite of Functions to Perform Uniform Sampling of a Sphere*, Mathworks File Exchange. [Available at https://www.mathworks.com/matlabcentral/fileexchange/37004-suite-of-functions-to-perform-uniform-sampling-of-a-sphere, accessed 2017.]
Shure, L., R. L. Parker, and G. E. Backus (1982), Harmonic splines for geomagnetic modelling, *Phys. Earth Planet. Inter.*, *28*(3), 215–229, doi:10.1016/0031-9201(82)90003-6.
Simons, F., F. Dahlen, and M. Wieczorek (2006), Spatiospectral concentration on a sphere, *SIAM Rev.*, *48*(3), 504–536, doi:10.1137/S0036144504445765.
Smoluchowski, R. (1975), Jupiter's molecular hydrogen layer and the magnetic field, *Astrophys. J.*, *200*, L119–L121.
Stockmann, R., C. C. Finlay, and A. Jackson (2009), Imaging Earth's crustal magnetic field with satellite data: A regularized spherical triangle tessellation approach, *Geophys. J. Int.*, *179*(2), 929–944, doi:10.1111/j.1365-246X.2009.04345.x.
Tibshirani, R., J. Bien, J. Friedman, T. Hastie, N. Simon, J. Taylor, and R. J. Tibshirani (2010), Strong rules for discarding predictors in lasso-type problems, *J. R. Stat. Soc., Ser. B*, *74*, 245–266.
Zou, H., and T. Hastie (2005), Regularization and variable selection via the elastic net, *J. R. Stat. Soc., Ser. B*, *67*(2), 301–320, doi:10.1111/j.1467-9868.2005.00503.x.